ARTICLE

Continuous borehole optical televiewing reveals variable englacial debris concentrations at Khumbu Glacier, Nepal

Katie E. Miles [1✉], Bryn Hubbard [1], Evan S. Miles [2], Duncan J. Quincey [3], Ann V. Rowan [4], Martin Kirkbride [5] & Josephine Hornsey[4]

Surface melting of High Mountain Asian debris-covered glaciers shapes the seasonal water supply to millions of people. This melt is strongly influenced by the spatially variable thickness of the supraglacial debris layer, which is itself partially controlled by englacial debris concentration and melt-out. Here, we present measurements of deep englacial debris concentrations from debris-covered Khumbu Glacier, Nepal, based on four borehole optical televiewer logs, each up to 150 m long. The mean borehole englacial debris content is $\leq 0.7\%$ by volume in the glacier's mid-to-upper ablation area, and increases to 6.4% by volume near the terminus. These concentrations are higher than those reported for other valley glaciers, although those measurements relate to discrete samples while our approach yields a continuous depth profile. The vertical distribution of englacial debris increases with depth, but is also highly variable, which will complicate predictions of future rates of surface melt and debris exhumation at such glaciers.

[1] Centre for Glaciology, Department of Geography and Earth Sciences, Aberystwyth University, Aberystwyth, UK. [2] Swiss Federal Research Institute WSL, Birmensdorf, Switzerland. [3] School of Geography, University of Leeds, Leeds, UK. [4] Department of Geography, University of Sheffield, Sheffield, UK. [5] Department of Geography and Environmental Science, University of Dundee, Dundee, UK. ✉email: kam64@aber.ac.uk

The importance of glacier meltwater in contributing to global water resources and moderating seasonal streamflow variations is widely recognised, particularly for catchments draining High Mountain Asia[1–4]. However, the shrinking of glaciers in response to a warming climate[5] raises concerns over their longevity and contribution to future water resources[1,4]. For example, the passing of 'peak water' is predicted to occur across High Mountain Asia before the end of this century, after which glacial inputs to streamflow will diminish rapidly[1,6,7]. As a result, the potential impact of climatic changes on these basins is becoming increasingly apparent; in a global study of 78 'water towers', the three most vulnerable were located in High Mountain Asia[8].

The rate of atmospherically driven surface melting at debris-covered glaciers, which comprise ~30% of glacial ablation areas in High Mountain Asia[5], is strongly influenced by the spatially variable supraglacial debris thickness, described by the shape of the Østrem curve[9]. Where debris layers are thin, melt rates are enhanced compared to debris-free ('clean-ice') surfaces, peaking at the 'effective thickness', a value of the order of 0.02–0.05 m according to local conditions. As the debris layer thickens beyond this, it reaches a 'critical thickness' of ~0.05 m at which the melt rate of the debris-covered ice is equal to that of clean ice. Above this critical thickness, the debris layer insulates the ice surface and suppresses, rather than enhances, atmospherically driven ablation[9–13]. Due to this melt suppression, debris-covered glaciers are expected to persist longer than climatically equivalent clean-ice glaciers[14], becoming increasingly important water stores as clean-ice glaciers disappear. Yet, recent studies have found glacier-scale thinning rates at debris-covered glaciers to be similar to those at clean-ice glaciers, referred to as the 'debris-cover anomaly'[15–19]. Importantly, as mass balance becomes more negative, supraglacial debris layers will increase in thickness and extend upglacier over time[20], primarily due to the enhanced exhumation of englacial debris[14,21–23], augmented by deposits from hillslopes and lateral moraines that will continue to contribute spatially and temporally discrete supplies[24–27]. Englacial debris will therefore play a key role in determining rates of ice loss, potentially insulating these important ice reserves for decades to come. However, despite its importance, no measurements of englacial debris concentration or distribution have yet been reported for any High Mountain Asian debris-covered glacier.

Our aim herein is to measure and report the first deep and spatially distributed englacial debris concentrations at a High Mountain Asian debris-covered glacier. We drilled by pressurised water[28] and logged by optical televiewer (OPTV)[29] four boreholes located across the ablation area of debris-covered Khumbu Glacier, Nepal Himalaya (Fig. 1), in 2017 and 2018 (Supplementary Table 1). The OPTV logs provide a geometrically accurate full-colour image of the complete borehole wall at a typical resolution of ~0.22 mm laterally and ~1 mm vertically, providing an effective means of identifying and quantifying inclusions[29] such as englacial debris. Here, we analyse these four OPTV image logs to map and quantify englacial debris concentrations at Khumbu Glacier.
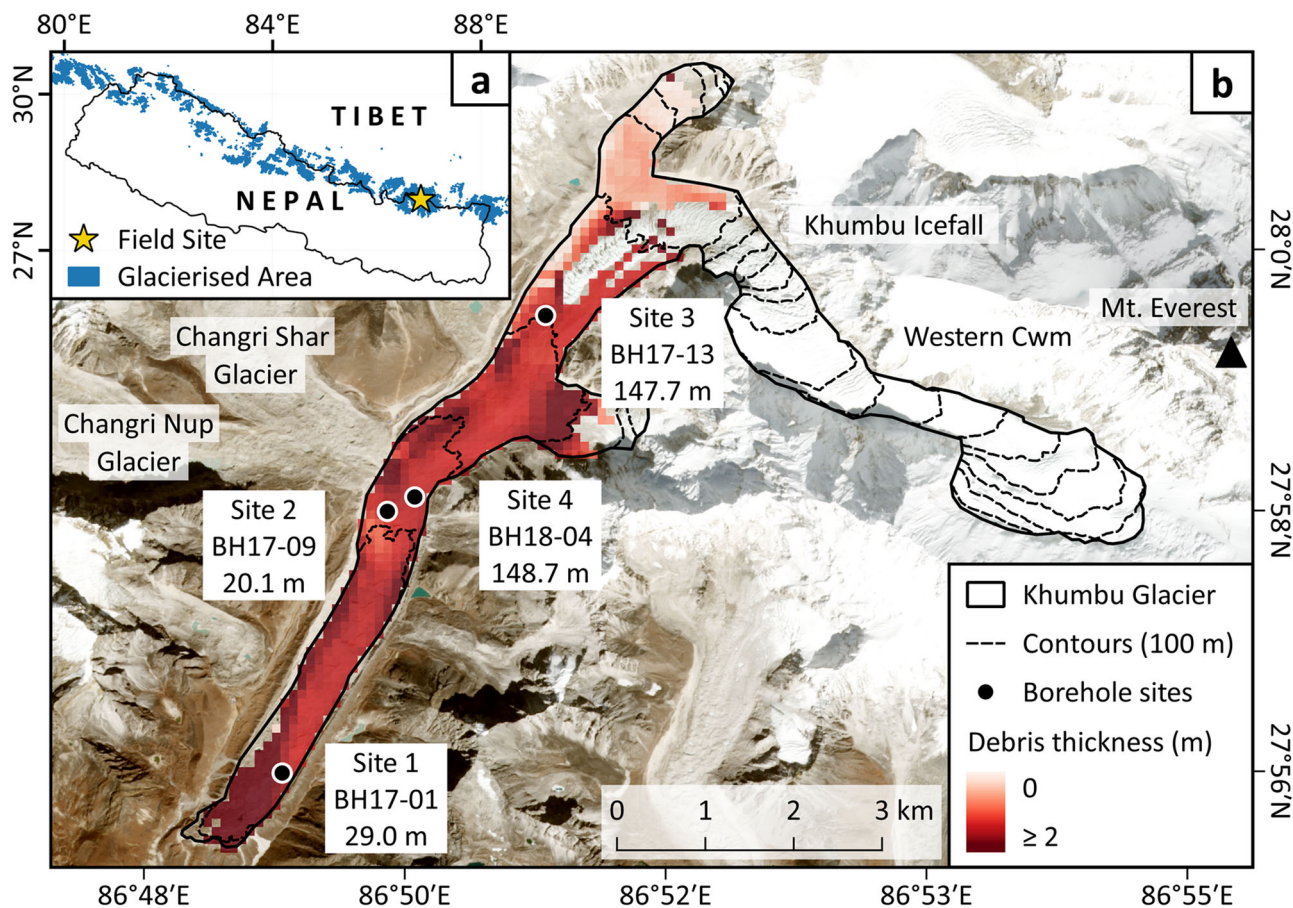
Fig. 1 Location of Khumbu Glacier and televiewed boreholes. a Location of Khumbu Glacier, Nepal. b Location of boreholes logged by optical televiewer on the glacier. The background is a Sentinel-2A image acquired on 30 October 2018. Glacier contours are at 100 m intervals from 4900 to 6800 m a.s.l., created from the 2015 SETSM DEM[57]. Supraglacial debris thicknesses are modelled outputs[27]. Each borehole is labelled with the site number, borehole ID[28,33,58], and OPTV log length[59].
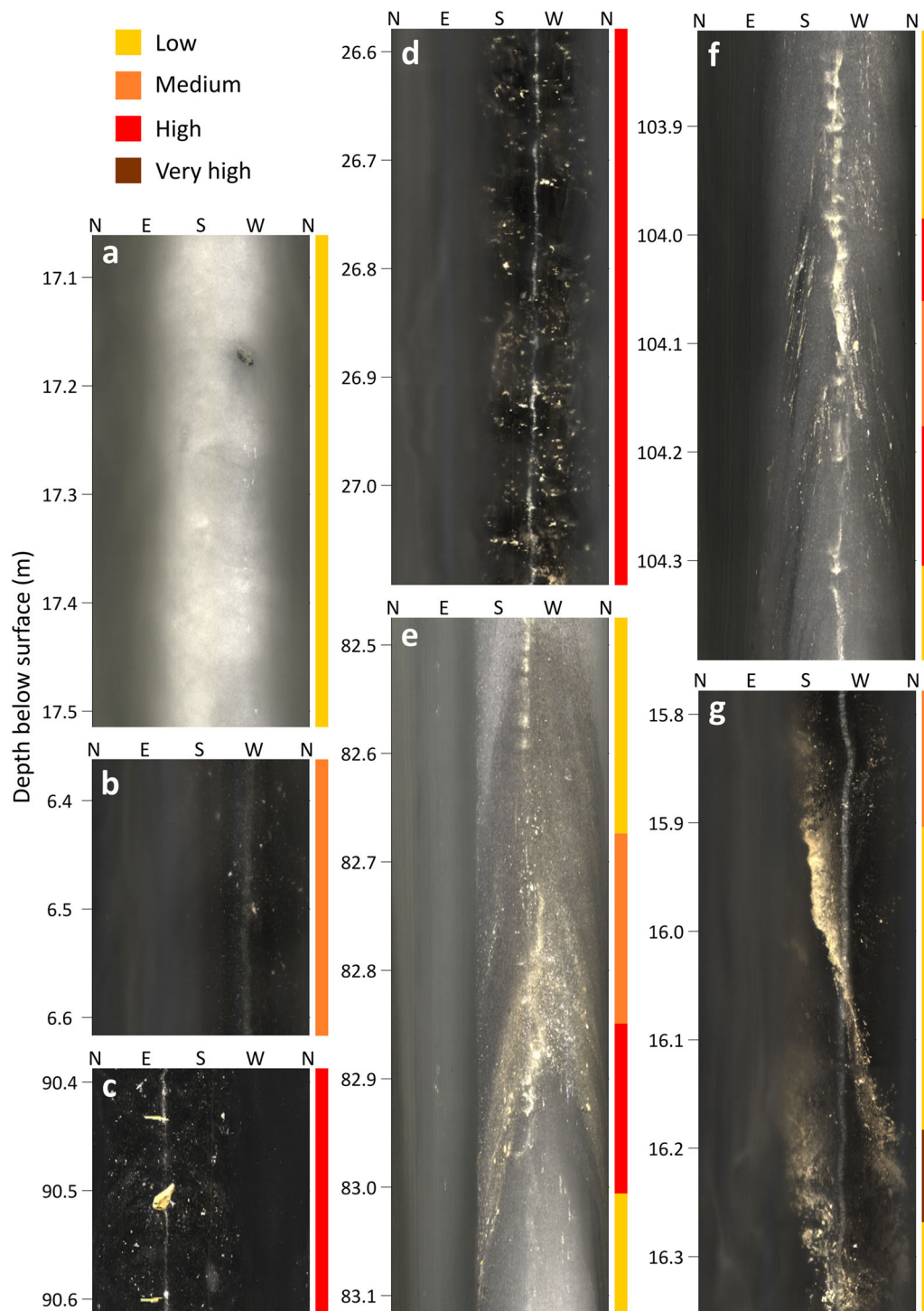
Fig. 2 Examples of OPTV image log debris inclusions and classifications (coloured bars). **a** A single large clast in BH17-09 (Site 2). **b** Fine debris and small clasts in BH17-01 (Site 1). **c** Large clasts and fine, dispersed sediment in BH18-04 (Site 4). **d** High concentration of small clasts in BH17-01 (Site 1). **e** A high concentration, discrete layer of fine sediment in BH17-13 (Site 3). **f** High concentration, discrete layers of small debris clasts, and fine sediment in BH17-13 (Site 3). **g** Very high concentration, discrete layers of fine sediment in BH17-01 (Site 1). All logs are unrolled to progress North-East-South-West-North from left to right. Saturated vertical reflections are superficial artefacts from the drilling process. Obscured parts of the images (i.e., **b** from N–S; **c** from SW–N; and **d**–**g** from N–SE) are due to turbid water (Supplementary Fig. 5 and 'Methods' section), and are excluded from all analysis.

Results

The OPTV successfully logged all four boreholes, totalling 345.5 m of the glacier's interior (full, raw image logs are shown in Supplementary Figs. 1–4). Two of the logs, at Sites 3 and 4 in the mid-ablation area, each reached ~150 m depth (Fig. 1b and Supplementary Table 1). Image quality was variable, with sectors often obscured by turbid borehole water and/or uneven borehole drilling[28] (Supplementary Fig. 5). However, debris was clearly visible in all the OPTV images as reflections brighter than the background ice, often with a lithologically controlled red-gold hue (Fig. 2). Debris distribution through the logs varied: fine sediment and discrete clasts were observed to be either dispersed

Table 1 Summary of borehole englacial debris concentrations and estimated ice column debris thickness, by site.

	Facies	Site 1	Site 2	Site 3	Site 4	Units
Low (0.0083% by volume)	1	26.8	98.1	88.2	95.6	% of OPTV image area
Medium (5.5% by volume)	2a	58.3	1.8	11.4	3.7	
High (15% by volume)	2b	13.0	0.2	0.5	0.7	
Very high (65% by volume)	3	1.9	0	0	0	
Mean borehole englacial debris concentration		**6.4**	**0.1**	**0.7**	**0.3**	**% by volume**
OPTV log length (visible image)		27.0	20.1	147.4	134.4	m
Equivalent debris layer thickness from borehole ice depth[a]		2.6	0.04	1.5	0.6	
Estimated full ice thickness[b]		46	225	337	252	
Equivalent debris layer thickness from estimated full ice thickness[a]		**4.4**	**0.4**	**3.5**	**1.2**	**m**

Uncertainties in the category debris concentrations, and therefore the mean borehole debris concentrations and thicknesses, are estimated to be ±50% (Methods). The estimates presented exclude basal debris or any additional debris layers, such as buried rockfall deposits, that could not be penetrated by the hot-water drill[28]. Bolding indicates key values derived by our analyses.
[a]Thickness of the supraglacial debris layer that would result from melting the borehole length or full ice column (as indicated), assuming no debris redistribution at the surface and a bulk effective porosity of 0.33 (ref. [31]). Calculations are provided the 'Methods' section.
[b]Ice thicknesses are model outputs[27], except for Site 1 where the neighbouring borehole was considered to have reached the bed[28,33]

through the ice column or focused in discrete bands (examples are shown in Fig. 2). The image resolution was such that textures and shadows were visible on some of the larger clasts ('Methods' section). Each log was classified manually according to debris concentration into four categories (Fig. 2 and 'Methods' section): low, medium, high, or very high. The debris content of the medium and high categories (mean of 5.5% and 15% by volume, respectively) was determined directly from the OPTV image logs ('Methods' section and Supplementary Fig. 6). This was not possible for the low and very high categories, for which debris concentrations (mean of 0.0083% and 65% by volume, respectively) were attributed on the basis of their visual similarity to ice facies that have already been identified, and whose debris concentrations have been ascertained by direct measurement[30] ('Methods' section). The full classification of each image log at 0.01 m vertical resolution is shown in Supplementary Fig. 7 and the percentage of each log in each category is presented in Table 1. Most of the imaged ice (≥88% at Sites 2–4; Table 1) hosted debris that comprised small, scattered clasts, and dispersed fine sediment of low concentration (Fig. 2), though some appeared at higher concentrations (Fig. 2c–g), either dispersed throughout the ice or concentrated as dipping layers (Fig. 2e–g).

The mean borehole englacial debris concentration at Sites 2–4 (Fig. 1b) was ≤0.7% by volume (Table 1). This contrasts markedly with the higher mean concentration (6.4% by volume) measured at Site 1, located near the glacier's terminus. Indeed, if the entire ice column at Site 1 were melted, a total debris thickness of 4.4 m would be released, which is higher than at any of Sites 2–4 (0.4–3.5 m thickness) despite the ~5x greater ice thickness at Sites 3 and 4 (Table 1). These debris thicknesses assume a bulk effective porosity of 0.33, as measured on neighbouring Ngozumpa Glacier, Nepal[31], and may be considered as equivalent because no account is taken of debris spreading or erosion at the surface.
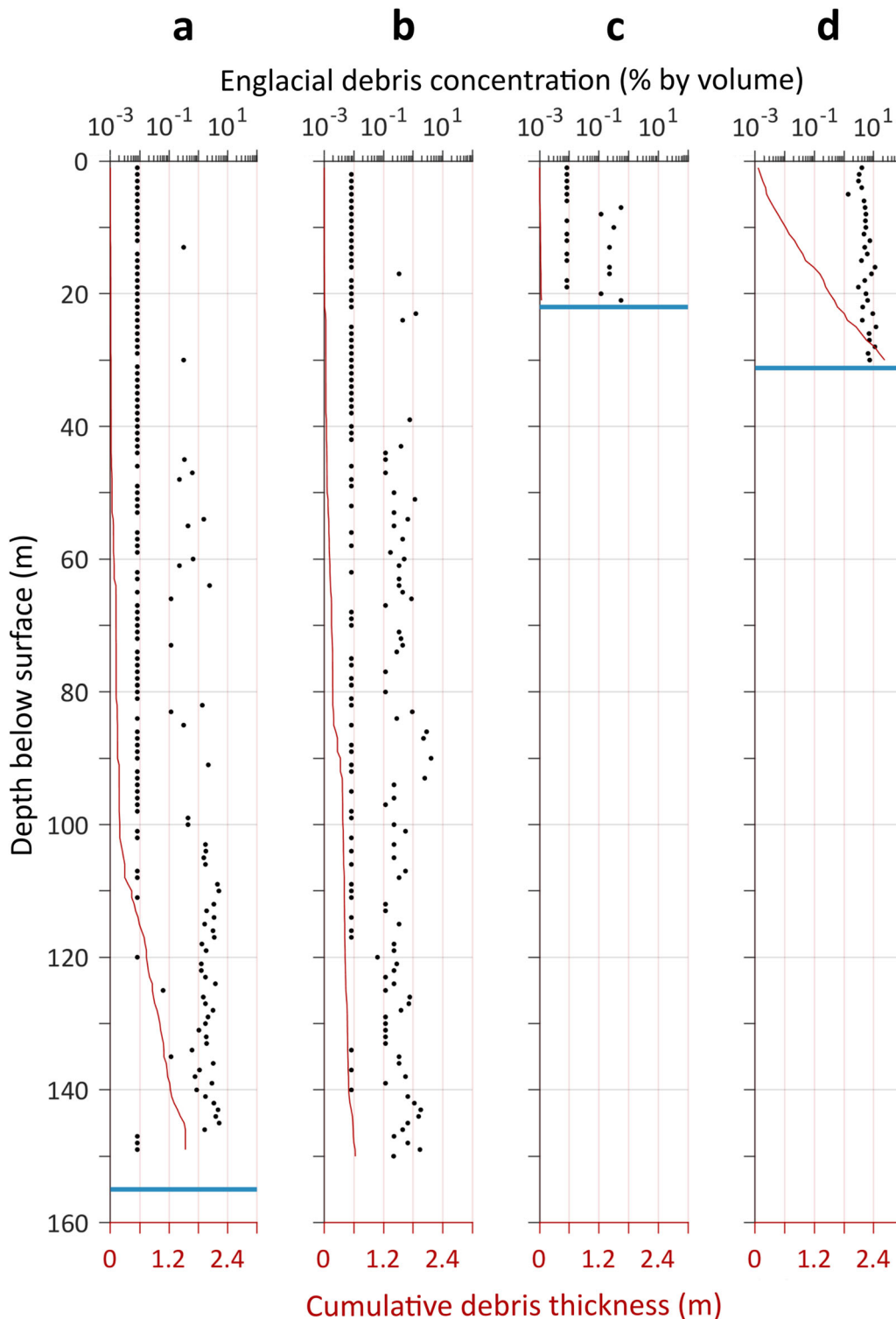
The englacial debris concentration profiles along each borehole are both highly variable and show a general increase in concentration with depth (Fig. 3). This is particularly evident in terms of the presence of relatively high local debris concentrations along the two longer boreholes: the lowermost 50 m of each of the OPTV image logs at Sites 3 and 4 contain 92% and 56% of the medium category layers, respectively (Fig. 3 and Supplementary Fig. 7). Similarly, the lower half of the boreholes at Sites 3 and 4 also host 73% and 84% of the high concentration debris layers, respectively. The impact of these higher concentration layers with depth is highlighted by the cumulative debris thickness curves (red lines on Fig. 3), which show an almost negligible increase between the surface and depths of ~100 and ~85 m at Sites 3 and 4, respectively. In contrast, Site 1 shows a strong increase in cumulative debris thickness along the full borehole length. This reflects the large number of medium category layers located throughout the borehole, augmented at depth by an increase in the presence of high and very high debris concentration categories: 86% and 96% of these layers were located in the lower half of the borehole, respectively.

Discussion

Technique evaluation. The OPTV image logs presented herein (Fig. 2 and Supplementary Figs. 1–4) yield unprecedented views at four locations into the interior of a high-elevation debris-covered glacier. Each log provides a continuous, geometrically consistent, and fine-resolution image from which englacial debris concentrations have been approximated (uncertainty is discussed below). Thus, relative to traditional sample-based methods, measurement of englacial debris concentration by borehole OPTV is less accurate, but has several other advantages. First, the raw data resolution is millimetric, enabling high-resolution variations in debris concentration to be identified and quantified. Second, precise debris disposition and association with structure is visible in the OPTV images (such patterns are not readily identifiable in surface samples, which are commonly melted in the field rather than returned to the laboratory for more precise analysis[32]). Third, OPTV-derived debris concentration profiles are continuous, and therefore free from bias introduced by selective surface sampling. Fourth, continuous OPTV-derived debris concentration profiles include subsurface ice that may not be accessible (for safety or other logistical reasons) when it is eventually exposed at the surface. Finally, the properties of a given ice–debris parcel will have changed during transport prior to exhumation. Consequently, although logistically demanding, borehole-derived englacial debris concentrations such as those we provide herein yield more spatially continuous—and hence representative—values of the volume and distribution of englacial debris than has previously been possible. To our knowledge, neither deep englacial debris concentrations nor the continuous variation of englacial debris with depth have hitherto been reported for any ice mass.

Despite the improvements noted above, calculating englacial debris concentrations from the analysis of OPTV image logs involves a higher level of uncertainty than does direct ice sampling. We consider the largest source of this uncertainty to be associated with the manual delineation and calculation of the areas of individual clasts, when determining the medium and high category concentrations ('Methods' section). This uncertainty was approximated through operator analysis of seven representative OPTV image samples of these two ice types. For

Fig. 3 Englacial debris concentrations plotted against depth for 1 m borehole sections from upglacier (left) to downglacier (right). a Site 3; **b** Site 4; **c** Site 2; and **d** Site 1. Black dots show the mean englacial debris concentration for each 1 m section of the borehole. Red lines show the equivalent cumulative debris thickness (assuming no debris spreading or erosion and a bulk porosity of 0.33)[31] that would be left if the ice above were to be melted (incrementing in the same 1 m sections), and thick blue lines represent the base of each borehole (Site 4 is at 192 m)[28]. The uppermost ~2 m of each borehole was not logged as this is the length of probe above the camera.

each sample, every identifiable debris clast was delineated, yielding a mean debris concentration of 5.5% (standard error 0.98%) for the medium debris concentration category and 15% (standard error 1.7%) for the high debris concentration category. In adopting published debris concentrations for our low and very high categories ('Methods' section), we take uncertainty to be the standard deviation of the multiple samples analysed by the original study[30] ('Methods' section).

Although the image log resolution was high (pixel size estimated to be ~0.22 laterally and 1 mm vertically), it was

insufficient to view individual scattered fine (≪1 mm) particles, likely resulting in an underestimation of the total debris concentration. However, our observations of ice forming supraglacial cliff faces across the tongue of Khumbu Glacier suggest that the scattered presence of fine debris is unlikely to be significant to the glacier's overall englacial debris concentration (in contrast to aggregations of such debris, which were visibly identifiable in the OPTV image logs, e.g., Fig. 2e, g). The debris concentration of the Site 4 image log may also be underestimated, as numerous small, saturated (i.e., all RGB channels at or close to maximum brightness (255)) reflections were interpreted as bubbles in the ice rather than as debris (which typically has a red-gold hue). It is possible for debris to appear as saturated reflections, but the shapes and clustering of the saturated reflections were more akin to bubbles than other clasts through the log, and were therefore classified as such.

Other sources of uncertainty include the occasionally poor quality of the OPTV image logs (turbid water obscuring the borehole wall in places; Supplementary Fig. 5) and the manual classification of the logs into one of the four debris categories. Furthermore, as only one of our boreholes may have reached the bed[28,33], all borehole debris concentrations are effectively lower limits of the glacier's net debris content, as they exclude debris entrained within basal ice and any additional layers too thick for the hot-water drill to penetrate, such as at Site 2 (ref. [28]).

Given the complexity of the uncertainties outlined above (and in the absence of accompanying deep ice cores that would allow direct quantitative comparison), we adopt a net uncertainty in our reconstructed debris concentrations at the borehole and facies scale of ±50% (including summary values shown in Table 1).

Englacial debris concentrations. The mean englacial debris concentrations measured along each borehole at Khumbu Glacier (0.1–6.4% by volume; Table 1) are generally higher than englacial debris concentrations measured - usually by discrete surface sampling - at glaciers elsewhere. While the low and very high debris categories were attributed published concentrations[30], the medium and high categories were calculated directly by OPTV image analysis. Assuming an ice density of 0.91 g cm^{-3} and a debris density of 2.2 g cm^{-3}, the medium category of 5.5% by volume equates to 12% by weight, and the high category of 15% by volume to 30% by weight. The mean borehole englacial debris concentrations we recorded at Khumbu Glacier were 14% by weight at Site 1; 0.31% by weight at Site 2; 1.7% by weight at Site 3; and 0.75% by weight at Site 4. All these values are higher than published englacial debris concentrations; for example, 0.0001–0.0097% by weight on the clean-ice Watts Outlet Glacier, Baffin Island, Canada[34], and 0.12% by weight on the debris-covered Djankuat Glacier, Caucasus[35] (both determined by surface measurements alone), and are closer to measured basal ice concentrations, which can range from 1–84% by weight[30,36]. Indeed, our very high category was assumed to have the same concentration as solid facies basal ice[30]; this category exists solely as a small number of discrete, high-density layers, which further suggests they may have been entrained at the bed, compared to the medium and high categories where the debris tends to be more dispersed.

While most ice-flow models of debris-covered glaciers do not consider englacial debris transport, the few that do either specify a uniform englacial debris content[23,35] or approximate it from considerations of the distribution of debris supplied to the glacier[14,27]. Our mean borehole englacial debris concentration at Site 3 (0.7% by volume) is similar to the mean englacial debris concentration of 0.6% by volume for the uppermost 145 m of the ice column at the base of the icefall yielded from Rowan et al.'s[27]

model of Khumbu Glacier. Their modelled glacier was fed by a constant debris input equivalent to an estimated headwall erosion rate of 1 mm a^{-1}. Our englacial debris concentrations are therefore within the range of values derived from estimates of headwall erosion at Khumbu Glacier, for example, 0.6 ± 0.3 mm a^{-1} for the present day (0.8 ± 0.2 mm a^{-1} during the Holocene) by Barker[37]. While our concentrations are higher than some published values, these likely underestimate englacial debris concentration. For example, one estimate[38] relied on inversion of the supraglacial debris volume and did not account for subsurface debris, while a second[25] based the erosion rate calculation on only one debris lithology.

Debris concentrations reconstructed along our boreholes are not uniform; instead, concentration increases with depth, particularly in terms of the frequency of high concentration layers (Fig. 3 and Supplementary Fig. 7). While this pattern would be expected at Site 1, where the base of the OPTV log is thought to be ~15 m above the bed and thus a basal influence is likely, the longer boreholes at Sites 3 and 4 extend through only ~50% of the ice column[33,39]. Higher debris concentrations at depth within Khumbu Glacier (and hence other similar glaciers) may result from a variety of processes, such as: (i) greater debris incorporation into the glacier in the upper than the lower accumulation area; (ii) debris falling to the base of crevasses in the glacier's icefall or at its margins; (iii) entrainment and elevation of basal debris within the glacier, such as in association with the icefall and its band ogives[26,40]; or (iv) tributaries (present or former) joining from hanging cirques/valleys leaving their basal debris layers in the lower sections of the main glacier tongue.

Englacial debris facies. Based on the debris concentration categories and their prevalence in the boreholes, we identify three material facies within Khumbu Glacier (Table 1) and discuss their likely sources. Facies 1 comprises the low category of predominantly fine, dispersed debris (Fig. 2), akin to the dispersed facies in otherwise 'clean' glacier ice reported at other valley glaciers[41]. This facies forms ≥88% of the borehole wall at Sites 2–4 and 27% at Site 1, and we therefore interpret this facies as the background matrix of ice at Khumbu Glacier. Due to its dispersed nature, the debris is most likely entrained in a spatially distributed manner during snow burial and firnification in the glacier's accumulation area[42], quite possibly associated with frequent minor mass movement events (e.g., rockfalls and avalanches) in Everest's Western Cwm (Fig. 1b).

We define facies 2 as the medium and high debris concentration categories of predominantly fine, scattered material of higher concentration than facies 1, with some larger clast sizes and banding of debris (e.g., Fig. 2c–f). We divide this facies into two sub-facies: facies 2a for the medium category extending through broad zones of our OPTV image logs, and facies 2b for the high category, in which some discrete debris bands are visible. The primarily scattered nature of the debris incorporated within this facies suggests a similar formation to facies 1, though infrequent thin bands of higher concentration debris could be the proximal edges of entrained mass movement deposits. The presence of isolated larger clasts deep in the ice column may be debris that has fallen into crevasses during transit through the icefall or, perhaps more likely, individual clasts that have been loosened by freeze–thaw cycles on rock slopes within the Western Cwm, dislodged and buried in the glacier's accumulation area during avalanches[43–45].

Facies 3, present only at Site 1, comprises the very high category of discrete layers of debris that is generally fine-textured, but includes some small clasts. The very high debris concentration of these layers (65% by volume; Table 1) is within the range

of reported basal debris layers[36,41], and although we did not record such layers in any other of our OPTV image logs, we observed debris-rich basal ice at the glacier surface near Site 2 (Supplementary Fig. 8). We therefore interpret facies 3 as layers of debris entrained at the bed and raised into an englacial position[42]. This concurs with observations of faceted and striated debris clasts—indicating erosion during former transport at the glacier bed[26]—in the supraglacial debris layer towards the glacier's terminus. Facies 3 forms only 1.9% of the Site 1 borehole ice column (Table 1), which may reflect the glacier's temperate basal interface in this area[33]; basal freeze-on of debris-laden material is more prevalent at cold-based glaciers or at a marginal warm-to-cold transition[46]. Regardless, the presence of these basal ice layers indicates that not all sediment has been removed from the glacier bed by meltwater, which is consistent with inferences of minimal subglacial drainage at Khumbu Glacier[47]. The glacier's terminus has previously been interpreted to sit on a raised bed of permeable sediment[37], which would allow percolation of some subglacial meltwater into the groundwater system[47] with only minor sediment entrainment.

We identify ~14 layers of facies 3 material in the Site 1 OPTV image. Consistent with the trend of increasing debris concentration with depth recorded at Sites 2–4, more of these layers are located deep in the borehole (Fig. 3): only one layer occurs in the uppermost 15 m of the OPTV image log, while ten are present in the lowermost ~10 m (Supplementary Fig. 7). The deepest layer is ~30.21 m from the surface, ~0.06 m above the base of the OPTV log, and an estimated 15 m above the glacier bed[28]. Some of the layers are closely spaced (e.g., two layers within ~0.02 m, and four layers occur within ~0.74 m) and may be single layers that have been subjected to intense deformation and isoclinal folding[48], but which would appear as separate layers in OPTV image logs. The mean dip of all facies 3 layers at Site 1 is 43.0°, with some layers dipping very steeply: for example, the layer illustrated in Fig. 2g dips upglacier at 74.1°. The depth, location, and angle of these layers is consistent with previous reports of thrusting[49], and we therefore interpret these layers as thrusts, resulting from basal shearing within the glacier's terminal region. There are several mechanisms by which such thrusting could occur at Khumbu Glacier, including: (i) velocity variations at the base of the icefall[50], where faster-moving ice departing the icefall is forced over slower-moving terminal ice; (ii) velocity variations at junctions with tributary glaciers[51]; and (iii) variations in basal conditions, such as a spatial[48] or temporal[52] change in thermal regime or the presence of a topographic barrier, such as a bedrock obstacle[46], a reverse in bed slope[53], or a proglacial debris apron[52].

We note that our estimates of englacial debris concentration at Khumbu Glacier (summarised in Table 1) do not include the presence of potentially debris-rich basal ice at the glacier bed (below the base of any of our upglacier boreholes at Sites 2–4), nor an unknown quantity of spatially discrete, thicker englacial deposits that our hot-water drill was unable to penetrate, as occurred at Site 2 (ref. [28]). Such layers could be larger mass movement deposits that were buried with the ice[54] in the Western Cwm or, at Site 2, debris delivered from Changri Shar and Changri Nup Glaciers (Fig. 1b) before their detachment from Khumbu Glacier. It is notable that no such deposits were intersected during any of the 760 m successfully drilled across all sites, nor terminated any boreholes at Sites 1, 3, and 4 (ref. [28]). Such debris layers therefore appear to be spatially restricted, consistent with an origin as avalanche and/or rockfall deposits from valley sidewalls, or as flood-related deposits from tributary glacier valleys[55].

We have quantified, for the first time, deep englacial debris concentrations and the continuous variation of englacial debris with depth for a High Mountain Asian debris-covered glacier

and, to our knowledge, for any ice mass. Even accounting for uncertainty, these reconstructed englacial debris concentrations are higher than point-based surface measurements made elsewhere on valley glaciers. The concentrations we record also increase with depth and are highly variable; both these properties have implications for future temporal evolution of surface melt and debris exhumation. We have identified three material facies within the glacier and noted evidence for basal debris being transported towards the surface in the lower ablation area of Khumbu Glacier. These results are important for building models of debris-covered glaciers, contributing to the robust representation of: (i) englacial debris transfer and deposition; (ii) surface energy balance and future evolution (particularly the development of the supraglacial debris layer and its influence on ablation); and (iii) ice motion, since the occurrence of basal shearing implies sediment incorporation and sliding upglacier of the point of initiation. Refinement of these processes in numerical models is necessary to forecast changes in the runoff of high-elevation debris-covered glaciers, and to project their impact on downstream discharge and the water supply to over 300 million people in the Ganges–Brahmaputra basin[8].

Methods

OPTV log acquisition. Boreholes were drilled using pressurised hot water; methods and borehole properties are provided in previous EverDrill publications[28,33]. At four sites (Fig. 1), a borehole was logged by an OPTV[29]: a 360° high-resolution camera that provides a true-colour, geometrically accurate, continuous image of the borehole wall. Borehole depths varied from 22–192 m, but the length of OPTV images was limited by the winch capacity of 150 m. Image logs begin at ~2 m depth below the surface (Supplementary Table 1), as this is the length of probe above the camera, and were taken of each borehole in both the down and up directions (Supplementary Table 1), with minimal notable difference between these images. The raw up-direction image logs are shown in full in Supplementary Figs. 1–4. All image logs were north-orientated and acquired at a logging speed of ~1 m min^{-1}, yielding a vertical image resolution of ~1 mm per pixel and a round-borehole image width of 1440 pixels[29]. Borehole diameter varies with depth, being widest at the surface and narrower at depth; for an estimated mean diameter of 100 mm, the horizontal image resolution is ~0.22 mm per pixel.

OPTV log processing. OPTV images for each borehole were collated and imported for analysis and presentation into WellCAD software. The Site 4 down log required depth adjustments to match the up log due to the OPTV sonde occasionally becoming stuck on debris protruding from the borehole wall; manual raising and lowering to free the sonde resulted in artificial jumps in depth. This did not affect any other log, including the Site 4 up-direction log.

OPTV log classification. Englacial debris visible in the OPTV logs was manually classified in WellCAD into 'low', 'medium', 'high', or 'very high' category bands (Fig. 2). Debris clasts included in the analysis were bright reflections with sharply defined outlines; patches that appeared to be clasts but were dark in colour and had blurred outlines were assumed to be recessed from the borehole wall and were omitted from all analysis. Automated classification was not possible due to the variability of debris reflections, the similarity between reflections from some debris and drilling artefacts on the borehole wall (Supplementary Fig. 5), and illumination differences between the logs. Sections where the borehole wall was obscured across the full image width by turbid water were omitted from the analysis (Supplementary Fig. 5). If only part of the width was obscured, the debris concentration of the unobscured side was assumed to be representative of the full width. The thickness of each debris concentration band was summed to yield the total length of each debris concentration category by borehole.

Category debris concentrations. Debris concentrations of the medium and high categories were determined by manually delineating all debris clasts within representative samples of each category in BIFAT software[56] (Supplementary Fig. 6). Seven sample sections of each category were selected from across the four up-direction logs. The resulting debris area was expressed as a percentage of the section area and averaged for each category, yielding a debris concentration by volume of 5.452% for medium (standard deviation 2.6%; standard error 0.98%) and 15.36% for high (standard deviation 4.4%; standard error 1.7%). This was not possible for the low and very high categories due to the prevalence of very fine, dispersed sediment, so these categories were assigned (on the basis of their visual similarity) ice facies reported from other valley glaciers[30,41]. The visual appearance of the low category at the glacier surface was most similar to 'clean glacier ice', which has an equivalent debris concentration of 0.0083% by volume; standard

deviation of 0.0041% by volume[30]. The visual appearance of the very high category (Supplementary Fig. 8) was most similar to 'solid facies ice', which has an equivalent debris concentration of 65% by volume; standard deviation of 79% by volume[30]. The debris concentrations of the low and very high categories, from Hubbard and Sharp[30], are means of samples from 11 glaciers in the Western Alps. All category concentrations are summarised in Table 1.

Borehole debris concentrations. The mean borehole debris concentration (C_{BH}, %) of the visible length of each borehole (L_{BH}, m) was calculated using the debris concentration (C_{cat}, %) and the total lengths (L_{cat}, m) of each category within each borehole:

$$C_{BH} = \frac{(C_{low} L_{low}) + (C_{med} L_{med}) + (C_{high} L_{high}) + (C_{Vhigh} L_{Vhigh})}{L_{BH}}.$$

The equivalent debris thickness in the borehole (Table 1), i.e., the depth of debris that would remain if the ice column were melted, was calculated by multiplying the mean borehole debris concentration by volume by the visible length of the OPTV log. This was extrapolated to the entire ice column at each borehole location by assuming the debris concentration measured in the borehole was applicable to the rest of the ice column. The mean borehole debris concentration was multiplied by the estimated ice column thickness (negating the unknown depth and debris concentration of any basal ice/debris layers), taken from model outputs[27] for all borehole locations except for Site 1, where the neighbouring borehole was considered to have reached the bed[28,33]. Equivalent supraglacial debris layer thicknesses (from both the borehole ice depth and full ice column depth) were calculated assuming a bulk effective porosity of 0.33, as measured on the neighbouring Ngozumpa Glacier, Nepal[31].

Data availability

References

1. Huss, M. & Hock, R. Global-scale hydrological response to future glacier mass loss. *Nat. Clim. Chang.* **8**, 135–140 (2018).
2. Immerzeel, W. W., van Beek, L. P. H. & Bierkens, M. F. P. Climate change will affect the Asian water towers. *Science.* **328**, 1382–1385 (2010).
3. Bolch, T. et al. in *The Hindu Kush Himalaya Assessment* (eds Wester, P., Mishra, A., Mukherji, A. & Shrestha, A. B.) 209–255 (Springer, Cham, 2019).
4. Pritchard, H. D. Asia's shrinking glaciers protect large populations from drought stress. *Nature* **569**, 649–654 (2019).
5. Kraaijenbrink, P. D. A., Bierkens, M. F. P., Lutz, A. F. & Immerzeel, W. W. Impact of a global temperature rise of 1.5 degrees Celsius on Asia's glaciers. *Nature* **549**, 257–260 (2017).
6. Hock, R. et al. in *IPCC Special Report on the Ocean and Cryosphere in a Changing Climate* (eds Pörtner, H. O. et al.) 202 (IPCC, 2019).
7. Rounce, D. R., Hock, R. & Shean, D. E. Glacier mass change in High Mountain Asia through 2100 using the open-source Python Glacier Evolution Model (PyGEM). *Front. Earth Sci.* **7**, 1–20 (2020).
8. Immerzeel, W. W. et al. Importance and vulnerability of the world's water towers. *Nature* **577**, 364–369 (2020).
9. Østrem, G. Ice melting under a thin layer of moraine, and the existence of ice cores in moraine ridges. *Geogr. Ann.* **41**, 228–230 (1959).
10. Kayastha, R. B., Takeuchi, Y., Nakawo, M. & Ageta, Y. in *Debris-Covered Glaciers* (eds Nakawo, M., Raymond, C. F. & Fountain, A.) 71–81 (International Association of Hydrological Sciences, 2000).
11. Nicholson, L. & Benn, D. I. Calculating ice melt beneath a debris layer using meteorological data. *J. Glaciol.* **52**, 463–470 (2006).
12. Collier, E. et al. Representing moisture fluxes and phase changes in glacier debris cover using a reservoir approach. *Cryosph.* **8**, 1429–1444 (2014).
13. Fyffe, C. L. et al. Processes at the margins of supraglacial debris cover: quantifying dirty ice ablation and debris redistribution. *Earth Surf. Process. Landforms* **45**, 2272–2290 (2020).
14. Anderson, L. S. & Anderson, R. S. Modeling debris-covered glaciers: Response to steady debris deposition. *Cryosphere* **10**, 1105–1124 (2016).
15. Gardelle, J., Berthier, E. & Arnaud, Y. Slight mass gain of Karakoram glaciers in the early twenty-first century. *Nat. Geosci.* **5**, 322–325 (2012).
16. Kääb, A., Berthier, E., Nuth, C., Gardelle, J. & Arnaud, Y. Contrasting patterns of early twenty-first-century glacier mass change in the Himalayas. *Nature* **488**, 495–498 (2012).
17. King, O., Bhattacharya, A., Bhambri, R. & Bolch, T. Glacial lakes exacerbate Himalayan glacier mass loss. *Sci. Rep.* **9**, 1–9 (2019).
18. Brun, F. et al. Heterogeneous influence of glacier morphology on the mass balance variability in High Mountain Asia. *J. Geophys. Res. Earth Surf.* **124**, 1331–1345 (2019).
19. Pellicciotti, F. et al. Mass-balance changes of the debris-covered glaciers in the Langtang Himal, Nepal, from 1974 to 1999. *J. Glaciol.* **61**, 373–386 (2015).
20. Kirkbride, M. P. & Warren, C. R. Tasman Glacier, New Zealand: 20th-century thinning and predicted calving retreat. *Glob. Planet. Change* **22**, 11–28 (1999).
21. Gibson, M. J. et al. Temporal variations in supraglacial debris distribution on Baltoro Glacier, Karakoram between 2001 and 2012. *Geomorphology* **295**, 572–585 (2017).
22. Kirkbride, M. P. & Deline, P. The formation of supraglacial debris covers by primary dispersal from transverse englacial debris bands. *Earth Surf. Process. Landforms* **38**, 1779–1792 (2013).
23. Glazyrin, G. E. The formation of ablation moraines as a function of the climatological environment. *Int. Assoc. Hydrol. Sci.* **104**, 106–110 (1975).
24. van Woerkom, T., Steiner, J. F., Kraaijenbrink, P. D. A., Miles, E. S. & Immerzeel, W. W. Sediment supply from lateral moraines to a debris-covered glacier in the Himalaya. *Earth Surf. Dyn.* **7**, 411–427 (2019).
25. Nakawo, M., Iwata, S., Watanabe, O. & Yoshida, M. Processes which distribute supraglacial debris on the Khumbu Glacier, Nepal Himalaya. *Ann. Glaciol.* **8**, 129–131 (1986).
26. Hambrey, M. J. et al. Sedimentological, geomorphological and dynamic context of debris-mantled glaciers, Mount Everest (Sagarmatha) region, Nepal. *Quat. Sci. Rev.* **28**, 1084 (2008).
27. Rowan, A. V., Egholm, D. L., Quincey, D. J. & Glasser, N. F. Modelling the feedbacks between mass balance, ice flow and debris transport to predict the response to climate change of debris-covered glaciers in the Himalaya. *Earth Planet. Sci. Lett.* **430**, 427–438 (2015).
28. Miles, K. E. et al. Instruments and methods: hot-water borehole drilling at a high-elevation debris-covered glacier. *J. Glaciol.* **65**, 882–832 (2019).
29. Hubbard, B., Roberson, S., Samyn, D. & Merton-Lyn, D. Digital optical televiewing of ice boreholes. *J. Glaciol.* **54**, 823–830 (2008).
30. Hubbard, B. & Sharp, M. J. Basal ice facies and their formation in the western Alps. *Arct. Alp. Res.* **27**, 301–310 (1995).
31. Nicholson, L. & Benn, D. I. Properties of natural supraglacial debris in relation to modelling sub-debris ice ablation. *Earth Surf. Process. Landforms* **38**, 490–501 (2013).
32. Hubbard, B. & Glasser, N. F. *Field Techniques in Glaciology and Glacial Geomorphology* (Wiley, Chichester, 2005).
33. Miles, K. E. et al. Polythermal structure of a Himalayan debris-covered glacier revealed by borehole thermometry. *Sci. Rep.* **8**, 1–9 (2018).
34. Dowdeswell, J. A. The distribution and character of sediments in a tidewater glacier, southern Baffin Island, N.W.T., Canada. *Arct. Alp. Res.* **18**, 45–56 (1986).
35. Bozhinskiy, A. N., Krass, M. S. & Popovnin, V. V. Role of debris cover in the thermal physics of glaciers. *J. Glaciol.* **32**, 255–266 (1986).
36. Kirkbride, M. P. in *Modern and past glacial environments* (ed Menzies, J.) 146–169 (Butterworth-Heinemann, 2002).
37. Barker, A. D. Glaciers, erosion and climate change in the Himalaya and St. Elias Range, SE Alaska. PhD Thesis, University of Washington (2016).
38. Banerjee, A. & Wani, B. A. Exponentially decreasing erosion rates protect the high-elevation crests of the Himalaya. *Earth Planet. Sci. Lett.* **497**, 22–28 (2018).
39. Gades, A., Conway, H., Nereson, N., Naito, N. & Kadota, T. in *Debris-Covered Glaciers*, Vol. 264 (eds Nakawo, M., Raymond, C. F. & Fountain, A.) 13–22 (International Association of Hydrological Sciences, 2000).
40. Goodsell, B., Hambrey, M. J. & Glasser, N. F. Formation of band ogives and associated structures at Bas Glacier d'Arolla, Valais, Switzerland. *J. Glaciol.* **48**, 287–300 (2002).
41. Hubbard, B., Cook, S. & Coulson, H. Basal ice facies: a review and unifying approach. *Quat. Sci. Rev.* **28**, 1956–1969 (2009).
42. Hambrey, M. J., Bennett, M. R., Dowdeswell, J. A., Glasser, N. F. & Huddart, D. Debris entrainment and transfer in polythermal valley glaciers. *J. Glaciol.* **45**, 69–86 (1999).
43. Scherler, D. Climatic limits to headwall retreat in the Khumbu Himalaya, eastern Nepal. *Geology* **42**, 1019–1022 (2014).
44. Nagai, H., Fujita, K., Nuimura, T. & Sakai, A. Southwest-facing slopes control the formation of debris-covered glaciers in the Bhutan Himalaya. *Cryosph.* **7**, 1303–1314 (2013).
45. Regmi, D. & Watanabe, T. Short communication: rockfall activity in the Kanchenjunga Area, Nepal Himalaya. *Permafr. Periglac. Process.* **20**, 390–398 (2009).

46. Boulton, G. S. On the origin and transport of englacial debris in Svalbard glaciers. *J. Glaciol.* **9**, 461–465 (1970).

47. Miles, K. E. et al. Surface and subsurface hydrology of debris-covered Khumbu Glacier, Nepal, revealed by dye tracing. *Earth Planet. Sci. Lett.* **513**, 176–186 (2019).

48. Hambrey, M. J. & Huddart, D. Englacial and proglacial glaciotectonic processes at the snout of a thermally complex glacier in Svalbard. *J. Quat. Sci.* **10**, 313–326 (1995).

49. Hambrey, M. J., Dowdeswell, J. A., Murrav, T. & Porter, P. R. Thrusting and debris entrainment in a surging glacier: Bakaninbreen, Svalbard. *Ann. Glaciol.* **22**, 241–X8 (1996).

50. Fushimi, H. Structural studies of glaciers in the Khumbu region. *Seppyo* **39**, 30–39 (1977).

51. Hewitt, K. Tributary glacier surges: an exceptional concentration at Panmah Glacier, Karakoram Himalaya. *J. Glaciol.* **53**, 181–188 (2007).

52. Evans, D. J. A. Apron entrainment at the margins of sub-polar glaciers, north-west Ellesmere Island, Canadian High Arctic. *J. Glaciol.* **35**, 317–324 (1989).

53. Glasser, N. F. & Hambrey, M. J. Sedimentary facies and landform genesis at a temperate outlet glacier: Soler glacier, North Patagonian Icefield. *Sedimentology* **49**, 43–64 (2002).

54. Dunning, S. A., Rosser, N. J., Mccoll, S. T. & Reznichenko, N. V. Rapid sequestration of rock avalanche deposits within glaciers. *Nat. Commun.* **6**, 1–7 (2015).

55. Miles, E. S. et al. Glacial and geomorphic effects of a supraglacial lake drainage and outburst event. *Nepal Himalaya. Cryosph.* **12**, 3891–3905 (2018).

56. Malone, T., Hubbard, B., Merton-Lyn, D., Worthington, P. & Zwiggelaar, R. Borehole and Ice Feature Annotation Tool (BIFAT): a program for the automatic and manual annotation of glacier borehole images. *Comput. Geosci.* **51**, 381–389 (2013).

57. Noh, M. J. & Howat, I. M. Automated stereo-photogrammetric DEM generation at high latitudes: surface Extraction from TIN-Based Search Minimization (SETSM) validation and demonstration over glaciated regions. *GIScience Remote Sens.* **52**, 198–217 (2015).

58. Hubbard, B., Miles, K. E., Quincey, D. J. & Miles, E. S. Summary of instrumentation installed in boreholes drilled into Khumbu Glacier, Nepal, in 2017 and 2018 as part of EverDrill research project [Data set]. *UK Polar Data Centre, Nat. Environ. Res. Counc. UK Res. Innov.* https://doi.org/10.5285/a7f28dea-64f7-43b5-bc39-a6cfcdeefbda (2019).

59. Hubbard, B., Miles, K. E. & Quincey, D. J. Borehole optical televiewer (OPTV) logs of boreholes drilled into Khumbu Glacier, Nepal, in 2017 and 2018 as part of EverDrill research project. *UK Polar Data Centre, Nat. Environ. Res. Counc. UK Res. Innov.* https://doi.org/10.5285/d80f5c86-89a7-46d6-8718-47e3d34ab368 (2019).

Author contributions

D.J.Q. conceived of and led, and B.H. and A.V.R. co-led, the EverDrill project. B.H. led the hot-water drilling, to which K.E.M., D.J.Q., and E.S.M. contributed. B.H. and K.E.M. carried out the OPTV logging. K.E.M. processed the data and wrote the manuscript. K.E.M., B.H., E.S.M., D.J.Q., A.V.R., M.K., and J.H. contributed to the data analysis and editing of the manuscript.

Competing interests

The authors declare no competing interests.

Additional information

Supplementary information is available for this paper at https://doi.org/10.1038/s43247-020-00070-x.

Correspondence and requests for materials should be addressed to K.E.M.

Peer review information Primary handling editors: Heike Langenberg.

Reprints and permission information is available at http://www.nature.com/reprints

Publisher's note Springer Nature remains neutral with regard to jurisdictional claims in published maps and institutional affiliations.